Energy Storage Materials 62 (2023) 102957

Contents lists available at ScienceDirect

Energy Storage Materials

journal homepage: www.elsevier.com/locate/ensm

Achieving stable interphases toward lithium metal batteries by a dilute and anion-rich electrolyte

Dandan Chai [a], Yazhen Zhu [a], Chaohong Guan [b], Tengxun Zhang [c], Shuai Tang [a], Hong Zhu [b], Xiang Li [a,*], Yongzhu Fu [a,*]

[a] College of Chemistry, Zhengzhou University, Zhengzhou, 450001, P. R. China
[b] University of Michigan-Shanghai Jiao Tong University Joint Institute, Shanghai Jiao Tong University, Shanghai, 200240, China
[c] School of Computer and Artificial Intelligence, Zhengzhou University, Zhengzhou, 450001, P. R. China

ARTICLE INFO

Keywords:
cluster
electrolyte design
low-concentration electrolyte
LiNO3 modulator
lithium metal battery

ABSTRACT

It is necessary to find an ideal electrolyte suitable for high performance lithium metal batteries (LMBs). Herein, we construct a novel cluster-like and anion-rich dilute electrolyte system by using $LiNO_3$ and trace lithium trifluoromethanesulfonate (LiOTf) in an ester-based electrolyte. In the designed system, NO_3^- is used as a modulator to regulate the coordination number of solvents and anions, and LiOTf is applied as a solubilizing agent of $LiNO_3$ and trigger for the generation of large cluster. As a result, an anion-regulated solvation structure (ARSS) is obtained even in a dilute Li-ion concentration (<1.5 M), evidenced by various techniques, enabling the electrolyte a high ion-conductivity which vastly differs from a high concentration electrolyte system. Afterwards, the ARSS facilitates the formation of an inorganic-rich solid electrolyte interface (SEI) on both cathode and anode, ensuring the LMBs high stability and long cycling performance.

1. Introduction

Lithium-ion batteries (LIBs) has the advantages of high specific capacity and long cycle life, which has been used in various energy storage systems[1,2]. Compared with the typical anodes in LIBs, lithium metal has the lowest electrochemical potential (-3.040 V versus the standard hydrogen electrode) and high theoretical specific capacity of 3860 mAh g^{-1}, making lithium metal batteries (LMBs) high energy density with potential for commercialization[3–5]. However, LMBs are hampered by dendrite growth and low coulombic efficiency (CE) issues of the lithium metal anode due to interfacial instability[6].

Various explorations have been made to address the problem of the interface between lithium metal and electrolyte[7–10]. An electrolyte engineering has been confirmed to be effective, such as electrolyte additives[11–15]. It is well known that the interfacial chemistry is inextricably linked to the solvation structure of the electrolyte. For a typical dilute electrolyte, the solvents have large ionic-dipole interaction with lithium ions, constructing a classical solvent-dominated solvation model (Figure 1a). The coordinated solvents preferentially decompose[16,17], becoming the organic-rich components in the solid–electrolyte interphase (SEI) which cannot withstand the production of lithium dendrites and continuous parasitic reaction during lithium plating/stripping process[18]. It is noted that the inorganic compositions in SEI exhibit a high Young's modulus, restricting the growth of Li dendrites[19] and improving the stability of SEI[20]. An anion-rich solvation model is an effective method to increase the inorganic proportion in SEI, by adding more Li-salts to break the solvent-dominated environment and create more contact ion pairs (CIPs)/aggregates (AGGs), such as high-concentration electrolytes[21,22] (HCEs) and localized high-concentration electrolytes[23] (LHCEs). However, both systems endure poor wettability and high cost[24].

The solvated structure can be modified by tuning the solvents and Li-salt concentrations. As an effective approach, the application of anion regulation, however, has rarely been studied, with poor understanding of the fundamental rationales. To compete with the polar solvents, an anion with a high donor number (DN) should be considered. Lithium nitrate ($LiNO_3$) here is chosen due to a high DN (22) of NO_3^-, which is a good film-forming agent[25–32] and often used as an additive in various battery systems[33–35]. A solvent-poor and NO_3^--rich sheath can be theoretically obtained by introducing NO_3^- modulator especially in an ester-based electrolyte due to a strong interaction between NO_3^- and Li^+ and the low DN of the ester solvents (Figure 1b). Moreover, numerous

* Corresponding authors.
E-mail addresses: xli@zzu.edu.cn (X. Li), yfu@zzu.edu.cn (Y. Fu).

https://doi.org/10.1016/j.ensm.2023.102957
Received 24 July 2023; Received in revised form 18 August 2023; Accepted 6 September 2023
Available online 6 September 2023

CIPs/AGGs are acquired, which can fill with the inner Helmholtz plane (IHP) and suppress the decomposition of the solvents. For this purpose, a moderate NO_3^- is needed.

In this work, we propose an anion-regulated solvation structure (ARSS) and design the aimed dilute electrolyte system (NO_3^--rich and cluster-like) by adding a small amount of LiOTf as a solubilizer into a commercial electrolyte of 1.0 M $LiPF_6$ in EC/DEC (1:1 v/v). The electrolyte in our system is based on $LiNO_3$ in ester solvents with dilute concentration (<1.5 M), consisting of NO_3^--rich solvation structure and the large clusters which has not been before. Given the extremely low solubility in ester solvents of $LiNO_3$, the solubilizing agent LiOTf is confirmed as a trigger in the designed electrolyte system (hereafter denoted as LNO/LOTf system) to dissolve 80 times $LiNO_3$ which shows the strongest ability of solubility promoting as far as we know. We conclude an innovative precipitation-solubilization equilibrium mechanism in the LNO/LOTf system. The anion-regulated solvation structure constructs the inorganic-rich compositions for the formation of a robust SEI, which inhibits constant interfacial reactions. As results, the Li plating/stripping CE of Li||Cu half-cell in the LNO/LOTf electrolyte reaches 98.5% at a current of 0.4 mA cm^{-2} and a capacity of 0.8 mAh cm^{-2}. The NCM811||Li full cell has a high-rate capability and maintains high-capacity retention of 95.8% after 250 cycles at 2 C rate (1 C=180 mA g^{-1}).

2. RESULTS AND DISSCUTION

First, we compare the dissolution capability of $LiNO_3$ in an ester-based electrolyte. As shown in Figure S1, even 0.1 M $LiNO_3$ cannot be fully dissolved into the Blank electrolyte. By a flagrant contrast, 0.4 M $LiNO_3$ can be fully added into the Blank electrolyte with the assistance of only 5 mM LiOTf, consisting of a homogeneous solution. This solubilizer (5 mM LiOTf) helps dissolve 80 times $LiNO_3$ (0.4 M), which is the strongest solubilizing agent in an ester-based electrolyte to the best of our knowledge. For a clear comparison, the dissolution capability of the typical reported solubilizers is summarized in Figure 2a, with the dissolving $LiNO_3$ ability based on every coordination atom of the solubilizer. The detailed parameters of the solubilizers are listed in Table S1. It is obvious that the solubilizing ability of LiOTf is better than other agents (such as other OTf^- based salts and high DN value solvents), represented by an average of ligand atom in LiOTf corresponding to dissolving 27 times $LiNO_3$. Herein, what is the mechanism of the solubilizing ability of LiOTf by dissolving so many times of $LiNO_3$ in the ester-based electrolytes? It is reasonable that a new complicated structure based on NO_3^- is generated in the system triggered by OTf^-.

The structure was first investigated by ultraviolet and visible spectrophotometry (UV-vis) due to its sensitivity to a ligand and particle size. As shown in Figure 2b, the Blank electrolyte with only $LiNO_3$ is compared with LNO/LOTf electrolyte, with the curves obtained by diluting with the Blank electrolyte which was deducted as the baseline. A strong peak at ~ 220 nm is a symbol of NO_3^-[36]. It is evident that the UV absorption curve of LNO/LOTf electrolyte (a clear redshift) is different from that of the $LiNO_3$ only system, indicating the changes of electron energy level of NO_3^- in the solvated structure. Given that the polysulfides Li_2S_x shows a redshift when x increases in Li-S[37] and similar system, as well as some typical cluster chemistry system (Ag-cluster, etc[38–40].), the formation of a large cluster is speculated to account for this redshift in LNO/LOTf system. To further confirm the speculation, transmission electron microscopy (TEM) was applied to observe the cluster property of the Blank electrolyte with only $LiNO_3$ and LNO/LOTf electrolyte. In the TEM vision, a solution trends to form an AGG of ions (surrounded by the solvents). Figure 2c shows some separated circular particles in the Blank electrolyte with only $LiNO_3$, which are the symbol of an AGG. It is noted that each AGG is an individual, which has no relationship with others. It is clearer in color mappings of F and N in Figure 2d, which is selected from the area shown in Figure S2 (details for O and P element). The elements gather around one circle, forming an AGG. A sharp contrast appears for the LNO/LOTf electrolyte, shown in Figure 2e. The AGGs connect each other, forming a large cluster. The difference is evident compared with the separated AGGs in Figure 2c, which is more apparent in the element mappings (Figure 2f, selected from the area in Figure S3). The elemental distribution is uniform, filling the whole cluster.

At this point we have acquired the essential difference between the Blank electrolyte and LNO/LOTf electrolyte. To further obtain direct evidence of the cluster property in the LNO/LOTf electrolyte, time-of-flight mass spectrometry (TOF-MS) was performed. As shown in Figure 2g, a series of new peaks around 835.43 emerge, which is a symbol of isotopic structures. The mass/charge (m/z) ratio appeared at 835.43 belongs to the cluster of $[(9Li)(PF_6)(OTf)(3NO_3)(2EC)(DEC)]^{4+}$, which exhibits a remarkable comparison in the Blank electrolyte with

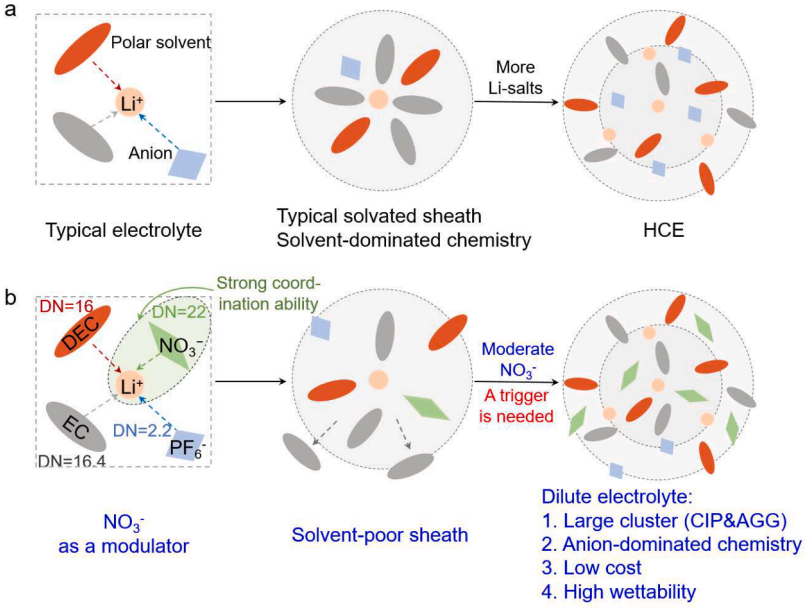

Figure 1. Design conception of the cluster-like and anion-rich dilute electrolyte. a) A conventional modification strategy from solvent-dominated solvated structure to an anion-rich structure. b) Design of an anion-rich solvated structure with large cluster in a dilute electrolyte by ARSS model.

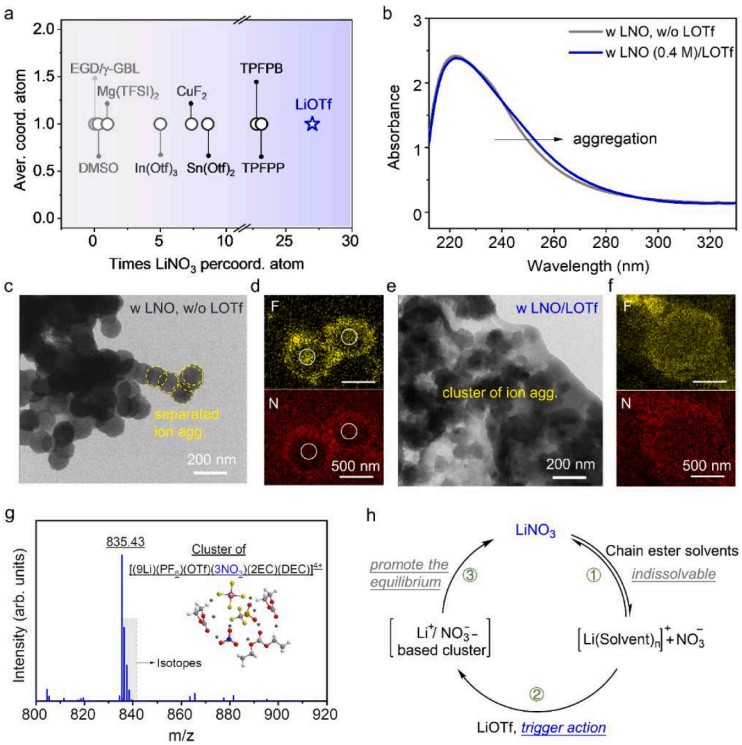

Figure 2. Cluster property in LNO/LOTf electrolyte triggered by LiOTf. a) Comparison of solubilization effect of different solubilizers in ester-based electrolyte. b) The UV-vis absorption curves of the Blank electrolyte with only $LiNO_3$ and LNO/LOTf electrolyte. c, d) TEM images and color mappings of F and N for the Blank electrolyte with only $LiNO_3$. e, f) TEM images and color mappings of F and N for LNO/LOTf electrolyte. g) TOF-MS analysis of the LNO/LOTf electrolyte. A clear peak appears indicating a large cluster. h) Solubilization promotion mechanism in LNO/LOTf electrolyte.

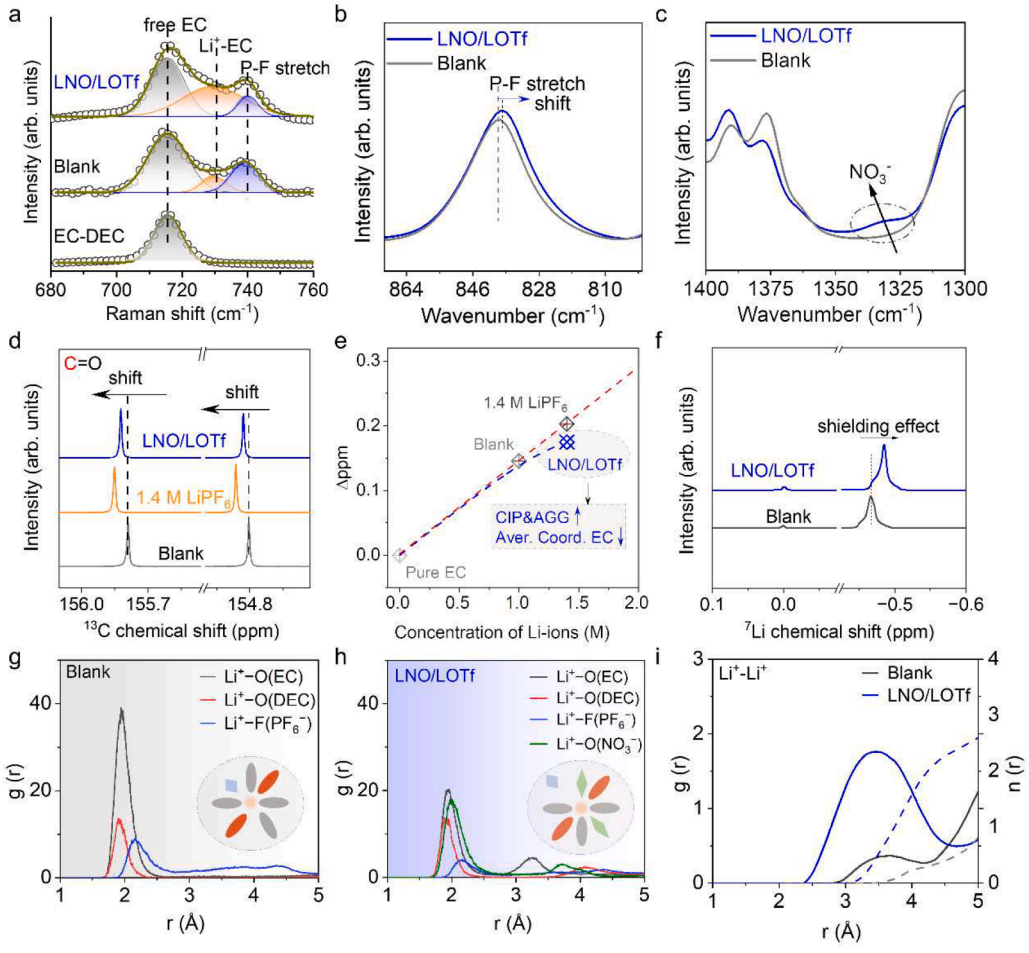

Figure 3. Solvated behavior of different electrolytes. a) Fitting results of Raman in Blank and LNO/LOTf electrolyte. b) The IR analysis of P-F in different electrolytes. c) The IR analysis of NO_3^- in different electrolytes. d) The ^{13}C NMR results in different electrolytes. e) The peak offset of the carbonyl carbon in EC as a function of Li-ions concentration. The location of pure EC is set as 0 ppm. f) The ^{7}Li NMR results in different electrolytes. g) Calculated RDF profiles for the Blank electrolyte. The schematic in the inset shows the corresponding solvated structure. h) Calculated RDF profiles for the LNO/LOTf electrolyte. i) Calculated RDF profiles (solid line) and coordination number (dash line) for the two systems, focusing on the relationship of Li^+-Li^+.

only $LiNO_3$ (see Figure S4). The results are the solid evidence that LiOTf can trigger the formation of a large cluster based on NO_3^-, endowed with the ability of dissolving generous $LiNO_3$.

A short summary is given in Figure 2h. It is known that $LiNO_3$ has a very limited solubility in an ester-based solvent (chain ester solvents, to be exact). The solution-precipitation equilibrium is displayed in equation 1 (Figure 2h), based on dissociation product of $[Li(solvent)n]^+$ and NO_3^-. The equilibrium is changed when adding LiOTf (as a trigger), inducing the recombination of Li^+ solvation structure to form a new and more stable solvated cluster structure based on multiple NO_3^- (equation 2). This means a decrease of $[Li(solvent)_n]^+$ part in equation 1, which can simultaneously promote the dissolution of $LiNO_3$ until reaching a new solution-precipitation equilibrium. As a result, the solubility of $LiNO_3$ is improved, which induces an anion-rich solvated structure helping the formation of a robust and inorganic-rich SEI.

To investigate the solvation behavior affected by the NO_3^- based cluster, the electrolytes were compared by using Raman spectroscopy, flourier transform infrared (FTIR) spectra and nuclear magnetic resonance (NMR) spectra. Figure 3a gives a clear comparison of the interaction among anions, cations, and solvents in the electrolyte. The peaks at 716 cm^{-1} and 731 cm^{-1} represent free EC and solvated EC (Li^+-EC), respectively. It is obvious that more Li^+-EC exists in the LNO/LOTf system (48% compared with 26% in the Blank electrolyte), as well as the DEC case in Figure S5, which is reasonable because more Li-salt ($LiNO_3$) was dissolved into the electrolyte. Meanwhile, the content of PF_6^- is reduced in the LNO/LOTf system because the relative concentration of PF_6^- is decreased. The stretching vibration of P-F at 740 cm^{-1} does not seem to have changed between the two systems in Raman spectra. However, FTIR result shows a difference in Figure 3b, represented by a redshift of P-F stretch in the LNO/LOTf system. It is known that the P-F stretch band at 845 cm^{-1} accounts for both separated ion pair (SSIP) and CIP. The redshift indicates more SSIP (for PF_6^-) is generated in the LNO/LOTf system[41], demonstrating a weaken binding of PF_6^- to a Li^+ due to the strong interaction between NO_3^- and Li^+. Afterwards, a clear peak at 1332 cm^{-1} appears in Figure 3c for the LNO/LOTf system, which corresponds to a N=O stretching vibration, indicating the successful dissolution of an ample amount of $LiNO_3$.

The solvation sheath structure was further probed in depth by ^{13}C and ^7Li NMR. In Figure 3d, the peaks at 155.79 ppm and 154.80 ppm in the Blank electrolyte represent the chemical shifts of carbonyl carbon in EC and DEC, respectively. Compared with the electrolyte with 1 M $LiPF_6$ (Blank), the carbonyl carbon of EC and DEC in 1.4 M $LiPF_6$ and LNO/LOTf electrolyte has a low-field shift, which is attributed to a lower electron cloud density, indicating an increased ion-dipole interaction between Li^+ and them[42]. Compared to the 1.4 M $LiPF_6$ system, the carbonyl carbon of the LNO/LOTf system (1.4 M Li^+) shifts to a high field, indicating a strong anionic effect. To obtain a clearer Li^+-solvated structure, the peak offset of carbonyl carbon in NMR was applied given a fact that the offset combines both the solvated and free solvents[41]. Figure 3e shows the peak offset for the carbonyl carbon of EC as a function of Li-ions concentration for different systems. The red dot line here is a criterion line, demonstrating a same Li^+-solvated environment represented by an equal proportion of solvated EC per Li-ion. For pure $LiPF_6$ system, the offset of 1.4 M $LiPF_6$ is exactly on the criterion line, indicating that the Li^+-EC in the Blank and 1.4 M $LiPF_6$ system are the same. In contrast, the offset for the LNO/LOTf electrolyte locates below the criterion line, indicating the increased CIPs/AGGs (more free EC). The DEC case is shown in Figure S6, which shows a similar CIPs/AGGs-tendency (more free DEC). Consequently, the LNO/LOTf system displays a solvated structure with a dilute characteristic (more free solvents) compared with $LiPF_6$ system at a same Li-ions concentration. Actually, the LNO/LOTf electrolyte has an adjacent ion-conductivity of 6.15 mS cm^{-1} which is comparable with the Blank electrolyte (6.48 mS cm^{-1}) and obviously higher than that (5.67 mS cm^{-1}) of 1.4 M $LiPF_6$ system (Table S2). A clear evolution of Li^+-solvated structure can be seen in ^7Li NMR spectra shown in Figure 3f. The peak has an obvious high-field shift, which may be attributed to the involvement of NO_3^- in the solvation sheath due to its stronger interaction with Li^+ than PF_6^-, as proved in the Raman results.

The radial distribution function (RDF) and coordination number of Li^+ calculated by Ab initio molecular dynamics (AIMD) further give the structure of the first solvated shell (r <3 Å) in different electrolytes. As shown in Figure 3g, the RDF profiles show that EC and DEC dominate the first solvated sheath with a handful of PF_6^- in the Blank system. In a sharp contrast, LNO/LOTf strongly affects the coordination structure, represented by an obvious decrease of EC and increase of NO_3^-. It is noted that NO_3^- ions easily enter the first solvated sheath and expel PF_6^- out of the sheath (Figure 3h), coinciding well with the Raman, NMR, and IR analysis. Moreover, the strong interaction of Li^+-NO_3^- forms an anion-rich cluster structure in the LNO/LOTf system, which potentially produces an anion-derived interfacial film. Furthermore, the RDF profiles give the information of Li^+-cluster, which is very important. As shown in Figure 3i, NO_3^- strengthens the interaction of Li^+-Li^+, evidenced by a shorter distance in the LNO/LOTf system. A weak peak appears in the RDF profile in the Blank system with an average coordination number close to 0.8. In contrast, a stronger signal appears in the LNO/LOTf system with an average coordination number close to 2.6. The results show that $LiNO_3$ is perfectly dissolved in the carbonate solvents and further confirm that more Li^+ ions are involved in the solvated shell in the LNO/LOTf system as a cluster characteristic.

In order to study the effect of the cluster-based electrolyte on Li metal anode, the Li||Li symmetric cells were compared for a galvanostatic test. As shown in Figure 4a, the overpotential of the LNO/LOTf system is gradually stabilized with the cycling time. In contrast, the overpotential of the Blank system keeps growing with time, indicating the severe side reaction and unstable SEI. Given that higher cycle capacity enables faster stabilization of the lithium anode and facilitates higher average CE of the battery[43], we applied a more accurate method of testing CE to evaluate the Li plating/stripping behavior (see supporting information for more details). As shown in Figure 4b, the LNO/LOTf system has significantly lower nucleation overpotential (67 mV) than the Blank system (87 mV) with a high CE of 98.5%, representing highly efficient Li plating/stripping behavior. In drastic contrast, the CE of the Blank system is only 77.1% because of severe irreversible capacity loss. The cycling performance also shows a huge difference in Figure S8, represented by a sharp decrease of the Blank system after only 30 cycles and a flat and stable behavior of the LNO/LOTf system. Figures 4c, d show the Li deposition morphology for the two systems by controlling a deposited capacity of 1 mAh cm^{-1}. There are obvious lithium dendrites produced in the Blank system. While the deposited lithium is relatively stout and block in the LNO/LOTf system, which is due to a reduced electrode/electrolyte contact area, reducing complex side reactions[44].

To further understand the composition of the SEI, X-ray photoelectron spectroscopy (XPS) test was conducted. Figures 4e-h show the XPS analysis of the lithium metal surface after cycles. The products in F 1s and P 2p spectra are derived from the decomposition of $LiPF_6$. In F 1s spectra, the signals of LiF (685.0 eV) and Li_xPF_y (687.1 eV) can be clearly detected in the Blank and LNO/LOTf systems[45]. An unknown new peak appears in the LNO/LOTf system at 683.2 eV, which may be a complex fluoride derived from the cluster structure. In P 2p spectra, the LNO/LOTf system has more inorganic product of PO_xF_y (133.8 eV)[45]. However, the Blank system has a high PF_5 component (136.6 eV), which is able to react with water to form a hazardous substance of HF[45]. In the LNO/LOTf system, the position of 398.4 eV (Figure 4g) indicates LiN_xO_y, representing the decomposition of nitrate[30]. As shown in Figure 4h, the Blank system has significantly obvious organic components, such as -CO_3- (289.0 eV), C=O (288.6 eV), and C-O (286.3 eV). Compared to the Blank system, the nascent inorganic component C-Li (282.7 eV) is present in the LNO/LOTf system[18]. The results show that the presence of various inorganic SEI components in the LNO/LOTf system benefit from the anion-rich and cluster-like electrolyte, which is profitable for the Li-ions transportation.

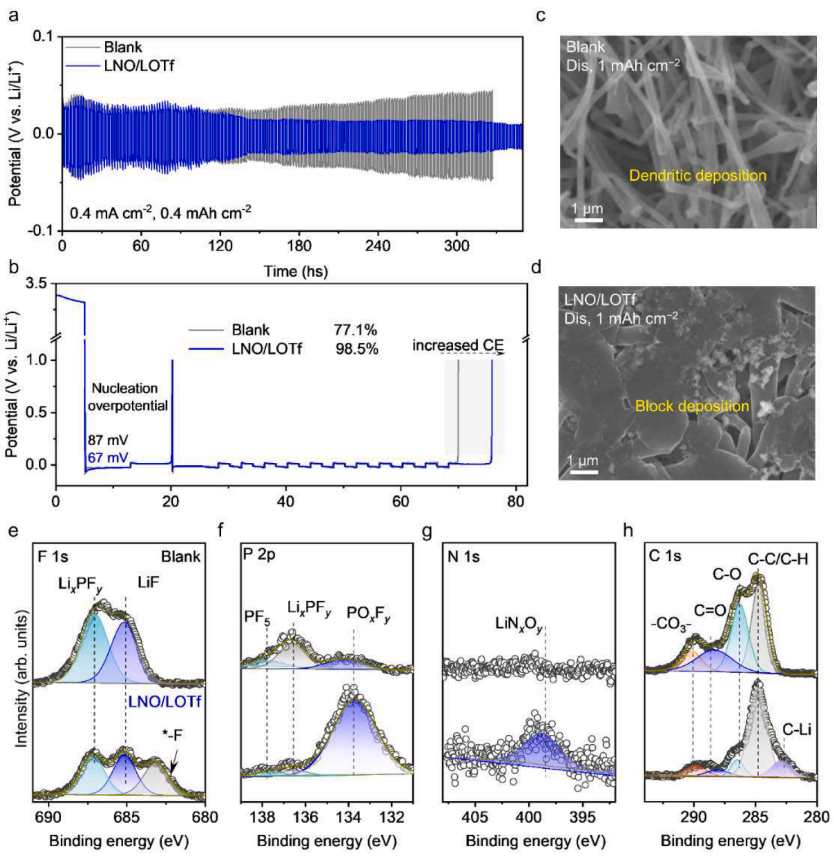

Figure 4. Characterization of the electrolyte on Li anode. a) The voltage profiles for Li||Li symmetrical cells with Blank and LNO/LOTf electrolyte at the current density of 0.4 mA cm^{-2} for 0.4 mAh cm^{-2}. b) Li plating/stripping behavior in Li||Cu cells with two electrolytes at a current density of 0.4 mA cm^{-2} and a capacity of 0.8 mAh cm^{-2}. c, d) The SEM images of the Li deposition morphology at 1 mA h cm^{-2} for the Blank and LNO/LOTf system, respectively. e-h) The XPS analysis for F 1s, P 2p, N 1s, and C 1s of Li anode after 200 cycles with two electrolytes, respectively.

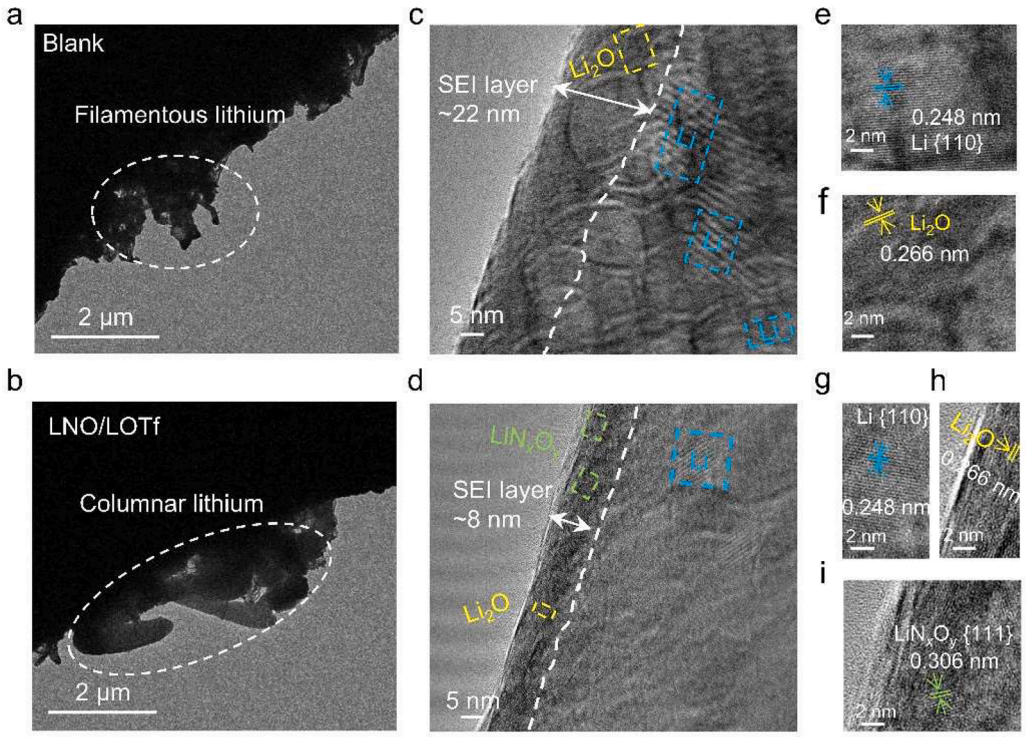

Figure 5. Cryo-TEM study on the SEI components for the two electrolyte systems. a, b) Morphology of lithium deposits in the Blank electrolyte and LNO/LOTf electrolyte, respectively. c, d) Enlarged TEM image of SEI with lattice structure in the Blank electrolyte and LNO/LOTf electrolyte, respectively. e, f) Details of the components in the SEI labeled in (c). g-i) Details of the components in the SEI labeled in (d).

To further understand the stereo-morphology of lithium metal and the SEI structure, we used cryogenic-transmission electron microscopy (Cryo-TEM) to obtain detailed information. From Figure 5a, it can be seen that the lithium metal deposited in the Blank system resembles intertwined filaments piled up at the edge of the copper grid. While the lithium metal deposited in the LNO/LOTf system is relatively bulky (Figure 5b). This buildup of large blocks is consistent with SEM results. From the enlarged figure, there is no obvious SEI boundary in the Blank system (Figure 5c). The thickness of this SEI is about 22 nm which can only be distinguished by finding the {110} plane of Li marked by the blue rectangle with a lattice distance of 0.248 nm and enlarged in Figure 5e. Meanwhile, the majority compositions of the SEI in the Blank system consist of amorphous components and Li_2O with a lattice parameter of 0.266 nm (yellow rectangle and enlarged in Figure 5f), which are due to the oxidative decomposition of the solvent. Differently, a denser and more uniform SEI (just about 8 nm) can be clearly seen in the LNO/LOTf system (Figure 5d), with enlarged lattice structures shown in Figures 5g, i. It can be seen that the SEI of the LNO/LOTf system is mostly inorganic components such as Li_2O and LiN_xO_y. Note that the component LiN_xO_y (with a lattice spacing of 0.306 nm marked by the green rectangle) coincides well with the XPS result (Figure 5g), which facilitates the conduction of lithium ions. This NO_3^--rich components dominate the SEI, achieving a robust interlayer with fast ion conductors and blocking the continuous parasitic reactions.

To evaluate the utilization of the electrolyte in the application of the traditional cathode, Li||NCM811 cells were chosen for the electrochemical performance. Figures 6a, b show the voltage decay behavior of the two systems. Compared with a fast voltage fade in the Blank system, the LNO/LOTf system delivers no detected voltage fade even after 200 cycles, demonstrating a robust and stable cathode. Figure 6c shows a comparison of the rate performance of the two systems. It can be seen that the LNO/LOTf system maintains a higher specific capacity than the Blank system at various rates, indicating better kinetics. Figure 6d shows the Li^+ diffusion coefficients calculated from the galvanostatic intermittent titration technique (GITT) results shown in Figure S9. It is obvious that the LNO/LOTf system has a higher Li^+ diffusion coefficient in the whole process compared with the Blank system. The Li^+ diffusion coefficient in the Blank system experiences a large fluctuation especially at ~ 4.0 V, evidencing an instable cathode electrolyte interphase (CEI). Meanwhile, the weakened interaction between Li^+ and solvents induced by NO_3^- enables a fast Li^+ de-solvation process and will be reflected in the rate performance. As results, the LNO/LOTf system exhibits an outstanding cycling performance at 2 C (Figure 6e). The capacity retention of the LNO/LOTf system maintains 95.8% after 250 cycles, with the average CE of 99.7%. Nevertheless, the Blank system experiences sharp capacity degradation, with a capacity retention of only 32.9% after 250 cycles. Inductively coupled plasma (ICP) test was performed to detect the solution of transition metals in the cathode after cycling. It can be seen that the dissolved Ni, Co, and Mn in the Blank system are much higher than those of the LNO/LOTf system (Figure S10), evidencing that a more stable CEI is formed in the LNO/LOTf system. Subsequently, the morphologies of NCM811 and Li anode after 1000 cycles are shown in Figures 6f, g, respectively. It can be clearly seen that the NCM811 surface in the Blank system has many cracks after 1000 cycles. While the cathode using LNO/LOTf electrolyte holds the integrity and has no detect crack in the view, indicating a

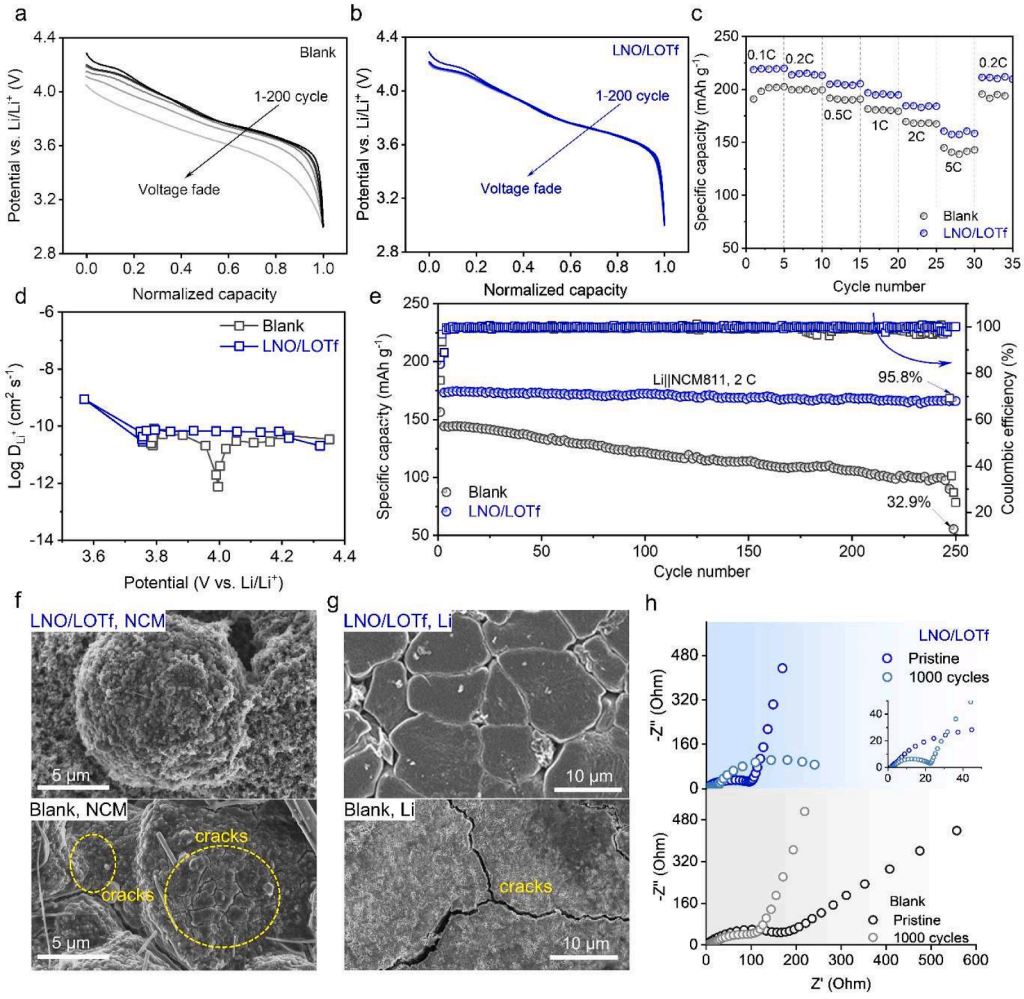

Figure 6. Electrochemical behavior and characterization of the cell. a, b) Voltage decay behavior of Li||NCM811 cells in Blank and LNO/LOTf electrolyte, respectively. c) Rate performance of Li||NCM811 cells using different electrolytes. d) The calculated Li^+ diffusion coefficient according to the GITT results from Figure S8. e) Cycling performance of Li||NCM811 cells at 2 C between 3-4.3 V. f, g) The morphologies of the cathode and Li anode after 1000 cycles in the Blank and LNO/LOTf electrolyte. h) EIS results of Li||NCM811 cells in the Blank and LNO/LOTf electrolyte.

robust CEI. The compositions of the CEI after cycling were also analyzed by XPS spectra (Figure S11).

The pronounced P signal appears in the LNO/LOTf system, with corresponding fitting results shown in Figure S12. There is more $Li_xPO_yF_z$ in the LNO/LOTf system, which is beneficial to promote the cyclic stability of the full cell[28]. In addition, the inorganic product LiN_xO_y is present in the LNO/LOTf system, produced by the decomposition of nitrate. Notably, a CEI is important for a cathode, which can maintain the stability of the cathode and is beneficial for the Li-ions transportation. Meanwhile, the uniform bulk lithium deposition is clear in Figure 6g for the LNO/LOTf system, ascribed from the anion-dominated characteristic of the electrolyte, which is favorable for Li plating/stripping. In a sharp contrast, there are deep and large cracks on the Li surface in the Blank system, which would continuously consume Li and electrolyte, destructing the anode. The results indicate that the cluster-like and anion-rich electrolyte has a positive effect on both anode and cathode. Furthermore, electrochemical impedance spectroscopy (EIS) measurement was applied for a resistance test, as shown in Figure 6h. The impedance of the Blank electrolyte is obviously larger than that of the LNO/LOTf system, evidencing an inferior compatibility between the Blank electrolyte and Li metal. After 1000 cycles, both systems have a decreased resistance. While the resistance of LNO/LOTf system is ~ 4 times smaller than that of the Blank system, which is attributed to the stable SEI/CEI formed in the cluster-like and anion-rich electrolyte.

3. Conclusion

In summary, we propose an ARSS model to construct a novel cluster-like and anion-rich dilute electrolyte system by using $LiNO_3$ and trace LiOTf in the ester-based electrolyte. A very important precipitation-solubilization equilibrium mechanism is elaborated in the $LiNO_3$-based ester electrolyte. The cluster characteristic in the designed electrolyte is carefully evidenced by UV, TEM, LC-MS, NMR, and AIMD. Each Li-ion coordinates higher proportion of anion in the cluster-like electrolyte compared with the Blank system, forming the inorganic-rich SEI components. As results, the Li plating/stripping behavior is regulated, forming bulk deposition instead of dendrites. Herein, a robust SEI is obtained, ensuring a high stability of the anode. The CE with LNO/LOTf electrolyte reaches 98.5% in a Li||Cu cell. Moreover, the Li||NCM811 cell in LNO/LOTf system maintains a capacity retention of 95.8% after 250 cycles at 2 C rate, with an average CE of 99.7%. While the capacity retention is only 32.9% for the Blank system. The LNO/LOTf electrolyte is beneficial for the stability of both anode and cathode. We hope our findings provide a new comprehension for the dilute electrolyte with anion-dominated solvation structure and pave a way for the design of novel electrolyte.

Author statement

Dandan Chai: electrochemical test, TEM, writing- original draft preparation. **Yazhen Zhu.**: Data curation. **Chaohong Guan**: DFT calculation. **Tengxun Zhang**: MS calculation. **Shuai Tang**: Validation. **Hong Zhu**: DFT calculation. **Xiang Li & Yongzhu Fu**: Supervision, Conceptualization, Methodology, Reviewing and Editing.

Declaration of Competing Interest

The authors declare that they have no known competing financial interests or personal relationships that could have appeared to influence the work reported in this paper.

Data availability

Data will be made available on request.

Acknowledgements

D.C., Y.Z., and C. G. contributed equally to this work. This work was supported by the National Natural Science Foundation of China (grant nos. 22005274 and 21975225) and The National Key R&D Program of China (2022YFB2402200).

Supplementary materials

Supplementary material associated with this article can be found, in the online version, at doi:10.1016/j.ensm.2023.102957.

References

[1] A. Manthiram, ACS Cent. Sci. 3 (2017) 1063–1069.
[2] M. Li, J. Lu, Z. Chen, K. Amine, Adv. Mater. (2018), e1800561.
[3] W. Xu, J. Wang, F. Ding, X. Chen, E. Nasybulin, Y. Zhang, J.-G. Zhang, Energy Environ. Sci. 7 (2014) 513–537.
[4] D. Lin, Y. Liu, Y. Cui, Nat. Nanotechnol. 12 (2017) 194–206.
[5] C. Fang, J. Li, M. Zhang, Y. Zhang, F. Yang, J.Z. Lee, M.H. Lee, J. Alvarado, M. A. Schroeder, Y. Yang, B. Lu, N. Williams, M. Ceja, L. Yang, M. Cai, J. Gu, K. Xu, X. Wang, Y.S. Meng, Nature 572 (2019) 511–515.
[6] X.-B. Cheng, R. Zhang, C.-Z. Zhao, Q. Zhang, Chem. Rev. 117 (2017) 10403–10473.
[7] M. Zhao, X.-Y. Li, X. Chen, B.-Q. Li, S. Kaskel, Q. Zhang, J.-Q. Huang, eScience 1 (2021) 44–52.
[8] A.-L. Chen, N. Shang, Y. Ouyang, L. Mo, C. Zhou, W.W. Tjiu, F. Lai, Y.-E. Miao, T. Liu, eScience 2 (2022) 192–200.
[9] G. Liu, Z. Cao, P. Wang, Z. Ma, Y. Zou, Q. Sun, H. Cheng, L. Cavallo, S. Li, Q. Li, J. Ming, Adv. Sci. 9 (2022), e2201893.
[10] H. Zhang, L. Huang, H. Xu, X. Zhang, Z. Chen, C. Gao, C. Lu, Z. Liu, M. Jiang, G. Cui, eScience 2 (2022) 201–208.
[11] H. Zhang, G.G. Eshetu, X. Judez, C. Li, L.M. Rodriguez-Martínez, M. Armand, Angew. Chem. Int. Ed. 57 (2018) 15002–15027.
[12] X. Li, R. Zhao, Y. Fu, A. Manthiram, eScience 1 (2021) 108–123.
[13] J. Lian, W. Guo, Y. Fu, Journal of the American Chemical Society 143 (2021) 11063–11071.
[14] R. Zhao, X. Li, Y. Si, W. Guo, Y. Fu, ACS Appl. Mater. Interfaces 13 (2021) 40582–40589.
[15] W. Gu, G. Xue, Q. Dong, R. Yi, Y. Mao, L. Zheng, H. Zhang, X. Fan, Y. Shen, L. Chen, eScience 2 (2022) 486–493.
[16] Z. Li, H. Rao, R. Atwi, B.M. Sivakumar, B. Gwalani, S. Gray, K.S. Han, T.A. Everett, T.A. Ajantiwalay, V. Murugesan, N.N. Rajput, V.G. Pol, Nat Commun 14 (2023) 868.
[17] M. Mao, X. Ji, Q. Wang, Z. Lin, M. Li, T. Liu, C. Wang, Y.S. Hu, H. Li, X. Huang, L. Chen, L. Suo, Nat Commun 14 (2023) 1082.
[18] S. Liu, X. Ji, N. Piao, J. Chen, N. Eidson, J. Xu, P. Wang, L. Chen, J. Zhang, T. Deng, S. Hou, T. Jin, H. Wan, J. Li, J. Tu, C. Wang, Angew. Chem. Int. Ed. 60 (2021) 3661–3671.
[19] X. Fan, X. Ji, F. Han, J. Yue, J. Chen, L. Chen, T. Deng, J. Jiang, C. Wang, Sci. Adv. 4 (2018) eaau9245.
[20] T.D. Pham, A. Bin Faheem, K.-K. Lee, Small 17 (2021), 2103375.
[21] X. Ren, L. Zou, S. Jiao, D. Mei, M.H. Engelhard, Q. Li, H. Lee, C. Niu, B.D. Adams, C. Wang, J. Liu, J.-G. Zhang, W. Xu, ACS Energy Lett 4 (2019) 896–902.
[22] H. Lu, C. Yang, F. Wang, L. Wang, J. Zhou, W. Chen, Q.-H. Yang, Nano Res (2022).
[23] Z. Wu, R. Li, S. Zhang, L. lv, T. Deng, H. Zhang, R. Zhang, J. Liu, S. Ding, L. Fan, L. Chen, X. Fan, Chem (2022).
[24] M.S. Ding, A. von Cresce, K. Xu, J. Phys. Chem. C 121 (2017) 2149–2153.
[25] X. Li, S. Guo, H. Deng, K. Jiang, Y. Qiao, M. Ishida, H. Zhou, J. Mater. Chem. A 6 (2018) 15517–15522.
[26] Q. Shi, Y. Zhong, M. Wu, H. Wang, H. Wang, Proc. Natl. Acad. Sci. U. S. A. 115 (2018) 5676–5680.
[27] J. Fu, X. Ji, J. Chen, L. Chen, X. Fan, D. Mu, C. Wang, Angew. Chem. Int. Ed. 59 (2020) 22194–22201.
[28] Y. Jie, X. Liu, Z. Lei, S. Wang, Y. Chen, F. Huang, R. Cao, G. Zhang, S. Jiao, Angew. Chem. Int. Ed. 59 (2020) 3505–3510.
[29] W. Zhang, Z. Shen, S. Li, L. Fan, X. Wang, F. Chen, X. Zang, T. Wu, F. Ma, Y. Lu, Adv. Funct. Mater. 30 (2020).
[30] W. Zhang, Q. Wu, J. Huang, L. Fan, Z. Shen, Y. He, Q. Feng, G. Zhu, Y. Lu, Adv. Mater. 32 (2020), e2001740.
[31] R. Zhao, X. Li, Y. Si, S. Tang, W. Guo, Y. Fu, Energy Storage Mater 37 (2021) 1–7.
[32] Y. Zhu, X. Li, Y. Si, X. Zhang, P. Sang, Y. Fu, J. Energy Chem. 73 (2022) 422–428.
[33] L. Zhang, M. Ling, J. Feng, L. Mai, G. Liu, J. Guo, Energy Stor. Mater. 11 (2018) 4–29.
[34] R. Xu, X. Shen, X.X. Ma, C. Yan, X.Q. Zhang, X. Chen, J.F. Ding, J.Q. Huang, Angew Chem Int Ed Engl 60 (2021) 4215–4220.
[35] J. Tan, M. Ye, J. Shen, Mater. Horizons 9 (2022) 2325–2334.
[36] L. Xu, Y. Sun, L. Gan, J. Han, P. Wang, L. Yu, X. Mei, W. Li, B. Lyu, C. Pei, W. Chu, Appl. Catal. B-Environ. 259 (2019), 117958.
[37] N. Xu, T. Qian, X. Liu, J. Liu, Y. Chen, C. Yan, Nano Lett 17 (2017) 538–543.
[38] L. He, J. Yuan, N. Xia, L. Liao, X. Liu, Z. Gan, C. Wang, J. Yang, Z. Wu, J. Am. Chem. Soc. 140 (2018) 3487–3490.

[39] J. Yan, S. Malola, C. Hu, J. Peng, B. Dittrich, B.K. Teo, H. Häkkinen, L. Zheng, N. Zheng, Nat. Commun. 9 (2018) 3357.
[40] X. Liu, G. Saranya, X. Huang, X. Cheng, R. Wang, M. Chen, C. Zhang, T. Li, Y. Zhu, Angew. Chem. Int. Ed. 59 (2020) 13941–13946.
[41] A.V. Cresce, S.M. Russell, O. Borodin, J.A. Allen, M.A. Schroeder, M. Dai, J. Peng, M.P. Gobet, S.G. Greenbaum, R.E. Rogers, K. Xu, Phys. Chem. Chem. Phys. 19 (2016) 574–586.
[42] S.J. Tan, Y.F. Tian, Y. Zhao, X.X. Feng, J. Zhang, C.H. Zhang, M. Fan, J.C. Guo, Y. X. Yin, F. Wang, S. Xin, Y.G. Guo, J. Am. Chem. Soc. 144 (2022) 18240–18245.
[43] B.D. Adams, J. Zheng, X. Ren, W. Xu, J.-G. Zhang, Adv. Energy Mater. 8 (2018), 1702097.
[44] G. Li, X. Duan, X. Liu, R. Zhan, X. Wang, J. Du, Z. Chen, Y. Li, Z. Cai, Y. Shen, Y. Sun, Adv Mater 35 (2023), e2207310.
[45] W. Yu, Z. Yu, Y. Cui, Z. Bao, ACS Energy Lett 7 (2022) 3270–3275.